PCCP

ROYAL SOCIETY OF CHEMISTRY

PAPER

View Article Online
View Journal | View Issue

Cite this: *Phys. Chem. Chem. Phys.*, 2025, **27**, 21593

Raman scattering and X-ray diffraction study of the temperature- and pressure-induced multistep spin transition in the complex $\{Fe^{II}(AnPy)_2[Ag^{I}(CN)_2]_2\}\cdot NO_2bz$

Yasmine Remili,[a] Maryam Nasimsobhan,[a] Rubén Turo-Cortés,[b] Laure Vendier,[a] Carlos Bartual-Murgui,[c] Gábor Molnár,*[a] Azzedine Bousseksou*[a] and José Antonio Real*[b]

Received 24th July 2025,
Accepted 9th September 2025

DOI: 10.1039/d5cp02831k

rsc.li/pccp

We acquired Raman spectra and X-ray diffraction (XRD) patterns across the temperature- and pressure-induced multistep spin transition in single crystals of the complex $\{Fe^{II}(AnPy)_2[Ag^{I}(CN)_2]_2\}\cdot NO_2bz$ (AnPy = 4-anthracenepyridine, NO_2bz = nitrobenzene). At the half transition plateau (*ca.* 200–220 K), previous work evidenced no superstructure or diffuse reflections in the XRD pattern, which could be indicative of spontaneous long- or short-range ordering of molecules in different spin states. Despite this lack of ordering, a distinct local symmetry breaking in the plateau is inferred from Raman spectroscopy in the present work, which revealed a complete extinction of several vibrational modes associated with the pure high spin and low spin states. We suggest that this local symmetry breaking does not transform into longer range order due to the positional disorder of NO_2bz guest molecules. The investigation was extended also to the high pressure behavior of the complex revealing a similar, stepped variation of lattice parameters with a plateau near 2–4 kbar, corresponding to *ca.* 50% transition, while the complete transformation to the LS form was achieved at *ca.* 6 kbar. The high pressure Raman spectra indicate local symmetry breaking in the plateau, which is closely comparable with the thermal transition behavior.

Introduction

The molecular spin crossover (SCO) phenomenon between the high spin (HS) and low spin (LS) configurations of $3d^4$–$3d^7$ transition metal ions, displayed by certain (pseudo-)octahedral coordination complexes, has been studied extensively in the past decades both from a fundamental point of view as well as for its potential applications.[1–5] At the molecular level the phenomenon is well understood on the basis of ligand field theory[6] and SCO systems with non-interacting molecules (*i.e.* solutions) can be then conveniently analyzed using straightforward thermodynamic considerations.[7] On the other hand, bulk SCO solids often display more intricate behaviors, which arise from the strong coupling between the spin state of the molecules and the structure of the crystal lattice. The most obvious manifestation of these couplings is evidenced by the plethora of thermal SCO curves, *i.e.* the plot of the high spin fraction (n_{HS}) *vs.* temperature. In bulk solids, these can be not only gradual (as in solutions), but also abrupt, can display hysteresis between the heating and cooling modes, can be incomplete and can exhibit two or more steps.[1] The differences in abruptness and the emergence of hysteresis can be rationalized in terms of cooperative interactions between the molecules. From a microscopic point of view, the cooperativity stems primarily from the large volume misfit between molecules of different spin states, giving rise to an elastic interaction energy,[8] which thus favors molecules in the same spin state. The volume strain associated with the spin state switching is also the principal reason for the coupling of the SCO phenomenon with other phase transitions, such as ferroelastic or order–disorder transitions, giving rise to crystallographic symmetry breakings at the intrinsically isostructural spin transitions.[9–11] Another intriguing aspect of solid-state SCO behavior is the occurrence of multistep spin transitions, characterized by two or more distinct steps (up to, at least, eight[12]), separated by plateaus. Reported as early as 1969,[13] this aspect of the SCO phenomenon has continued to draw attention of researchers – with the number of reported examples exploding in the past 10–15 years.

[a] *LCC, CNRS & University of Toulouse, 205 route de Narbonne, 31077, Toulouse, France. E-mail: gabor.molnar@lcc-toulouse.fr*
[b] *Departamento de Quimica Inorgánica, Instituto de Ciencia Molecular (ICMol), Universidad de Valencia, Catedrático José Beltrán 2, 46980, Paterna, Spain*
[c] *Departamento de Química Física, Universitat de València, Dr Moliner 50, Burjassot, 46100, Spain*

When discussing multistep SCO, first of all, one should underline that the steps do not reflect the occurrence of intermediate spin (IS) states: instead they signify the coexistence of HS and LS states. One must differentiate here the trivial case (class 1), wherein two (or more) nonequivalent metal sites are present in the lattice in both spin states. The ligand field (and structural parameters) being different at these sites, they will usually undergo SCO at different temperatures. A well characterized example for this behavior is provided by the compound $[Fe(btr)_3](ClO_4)_2$ (btr = (4,4′-bis-1,2,4-triazole)), wherein the two slightly different Fe(II) sites in the lattice undergo SCO at 222 K and 185 K, respectively, as observed using both ^{57}Fe Mössbauer spectroscopy and single-crystal XRD.[14] A more interesting situation is represented by compounds, which contain a unique SCO site (in one or both spin states), in which case the stepped transition must involve some symmetry breaking process (class 2). Among these compounds, we can further distinguish two main sub-classes depending on the existence or not of long-range ordering of HS and LS complexes.

The first sub-category concerns transitions, wherein molecules in the broken symmetry phase self-organize to form long-range ordered patterns of HS and LS sites (class 2a). The distinctive feature of these periodically modulated structures is the emergence of sharp superstructure reflections in the XRD pattern, which reflect a new periodicity in the crystal.[11,15] The prototypical example here is the complex $[Fe(2\text{-pic})_3]Cl_2{\cdot}EtOH$ (pic = picolylamine). The two-step SCO in this compound was discovered serendipitously in 1982,[16] but the definitive proof for the formation of a long-range ordered ''chessboard'' pattern of molecules in the plateau was provided by XRD only in 2003.[17] Besides this type of cell doubling, associated with a double symmetry breaking,[18] several other types of modulated structures (stripes and other patterns) have been reported in multistep compounds (coined also as spin-state concentration waves, SSCW[19]), whose wavevector can be either commensurate[20–31] or, less frequently, incommensurate[32–35] with respect to the underlying crystal lattice. In certain cases, more than one modulated structures (commensurate and/or incommensurate) were shown to appear through the spin transition, which has led to the analogy with the concept of Devil's staircase.[19]

The second sub-category (class 2b) covers stepped transitions, wherein local order (*e.g.* HS–LS pairs) appears in the intermediate phase(s), which is, however, not translated into a long-range modulated structure. In this case, no satellite reflections appear in the XRD pattern, but short-range order is manifested in certain cases by the emergence of a diffuse scattering signal.[35,36] The prototype compound of class 2b is the binuclear complex $[Fe(bt)(NCS)_2]_2bpym$ (bt = 2,2′-bi-2-thiazoline, bpym = 2,2′-bipyrimidine), which was the first purposefully designed two-step SCO compound.[37] ^{57}Fe Mössbauer[38] and Raman[39] spectroscopy measurements demonstrated that the plateau in the SCO corresponds to the formation of broken-symmetry HS–LS binuclear molecules, but XRD measurements showed only a random distribution of HS–LS and LS–HS molecules, without any long-range order.[40]

Arguably, the above classification of multistep SCO phenomena is subjective, such as the cited illustrations (for more examples, see the review of Ortega-Villar *et al.*[41]). For instance, several compounds can be categorized into more than one classes.[42] Further intricacies are related to the possibility of coupling the multistep SCO with other transitions and ordering phenomena.[36,43,44] In addition, stepped transitions may also arise due to finite size effects and the presence of inhomogeneities in the system.[45,46] It is worth noting also that the steps can be either gradual, associated with a homogeneous transformation, or hysteretic, associated with nucleation and growth processes.[47] This 'jungle' of complex ordering phenomena is also reflected by the large number of theoretical models developed to interpret the experimentally observed behaviors (and predict novel ones). To our best knowledge, the first model was proposed by Bari and Sivardiere in 1972 to interpret stepped spin transitions observed in transition metal oxides.[48] Further developments used a range of different methodologies with various refinements, such as thermodynamic models,[37,49,50] including regular-solution approaches[51] or the Landau theory of phase transitions,[52,53] as well as microscopic 'Ising-like'[18,54–56] or 'spring-ball'[46,57–59] models, and even a combination of these models with electronic structure calculations.[60] To put it simple, thermodynamic models (and microscopic models treated in the mean-field approximation) provide simple descriptions of the typical SCO behaviors using a small number of parameters, whereas microscopic models can provide a more in depth picture, but call for more-or-less complex numerical analysis (*e.g.* Monte Carlo simulations). Nevertheless, the basic aspects of the theory underlying the symmetry breaking in the most intriguing 'class 2' have been known since more than three decades, when the idea of antagonistic ferro- and antiferro-like elastic interactions was introduced[18] – in analogy with antiferromagnetic materials. This concept of opposed short-range (through bond) and long-range (through space) interactions, favoring either the formation of HS–LS pairs or pure (HS or LS) phases, respectively, continues to be the cornerstone of our understanding of symmetry-breaking multistep spin transitions.

In the past decade, thanks to the remarkable development of laboratory crystallography techniques, 'class 2a' transitions have been extensively studied both experimentally and theoretically, affording a highly sophisticated treatment.[11,15] In contrast, 'class 2b' transitions remain less investigated,[61] primarily for the difficulties of their experimental characterization. In the present paper, we examine the complex $\{Fe^{II}(AnPy)_2[Ag^{I}(CN)_2]_2\}{\cdot}NO_2bz$ (**1**) (AnPy = 4-anthracenepyridine, NO_2bz = nitrobenzene) belonging to this class of compounds. Complex **1**, as well as a series of similar compounds with formulae $\{Fe^{II}(AnPy)_2[M^{I}(CN)_2]_2\}{\cdot}Xbz$ (X = Ag or Au and X = NO_2, CH_3, Cl, Br or I), were reported by some of us previously.[62] With the exception of $AnPyAu{\cdot}CH_3bz$ and AnPyAu·Clbz, the different members of the family crystallize in orthorhombic structures, with a unique $Fe^{II}N_6$ site both in the HS and LS phases, wherein the iron center is coordinated to four equivalent equatorial $[M(CN)_2]^{2-}$ ligands and two axial AnPy ligands (Fig. 1a). Each equatorial ligand bridges two iron centers and therefore builds up infinite $\{Fe(AnPy)_2[M(CN)_2]_2\}$ two-dimensional (2D) layers. The bulky AnPy ligand promotes the generation of open structures, wherein the void space between

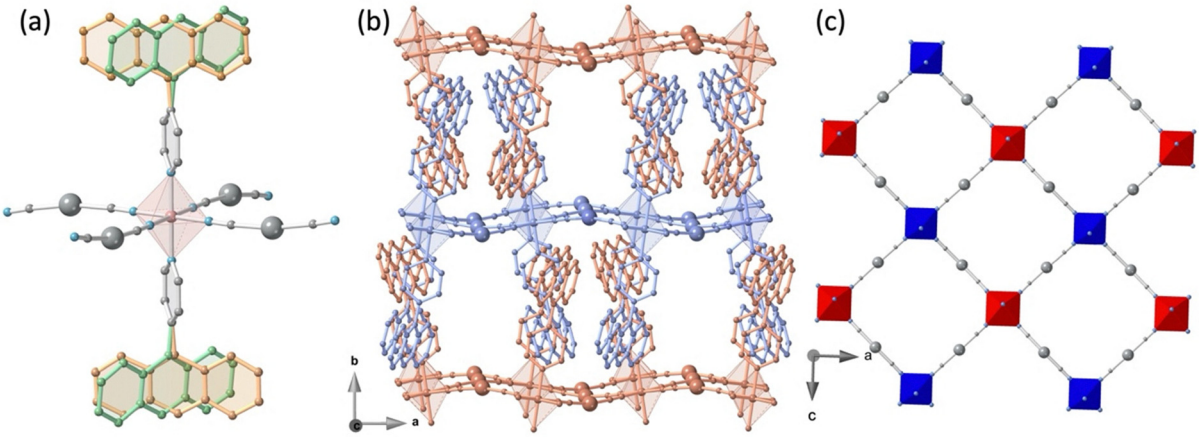

Fig. 1 Structure of AnPyAg·BzNO$_2$: (a) the coordination octahedron of the Fe(II) center, showing two possible orientations of the AnPy ligand. (b) Packing of three consecutive layers displaying the channels where the guest NO$_2$Bz molecules are located (these molecules are not shown because they are strongly disordered, and only one orientation of the AnPy ligand is shown). (c) 'Chessboard' of the HS (red) and LS (blue) iron centers observed in the plateau at half-transition for AnPyAg·ClBz, AnPyAg·BrBz and AnPyAu·BrBz.[62]

the layers allows for the inclusion of the Xbz guest molecules (Fig. 1b). Depending on the nature of the guest molecules, the compounds display different SCO temperatures, but share a common feature, which is the occurrence of a multistep SCO – typical for this family of dicyanometallic SCO frameworks.[12,29–31,63–66] Although in certain compounds, such as complex **1**, some of the steps cannot be resolved, in most cases four steps can be clearly distinguished, each corresponding to *ca.* 25% spin state conversion. Remarkably, the compounds AnPyAg·BrBz, AnPyAu·BrBz and AnPyAg·ClBz display a crystallographic transition, associated with the formation of two structurally independent HS and LS iron centers at the half-transition plateau, which form a regular "chessboard" within the 2D layers (Fig. 1c), exemplifying 'class 2a' stepped SCO behavior. In contrast, no symmetry breaking was observed in the compounds AnPyAg·NO$_2$Bz, AnPyAg·CH$_3$Bz and AnPyAu·NO$_2$Bz, for which the half-transition plateau is characterized by a mixture of HS and LS iron sites without any long range ordering, and which can therefore be ascribed to 'class 2b'-type stepped spin transitions.

With the aim to get further insight into the nature of this latter phenomenon, we conducted a Raman spectroscopic study on compound AnPyAg·NO$_2$Bz (**1**), which we report herein. The use of Raman spectroscopy is particularly interesting in this context, because it can reveal the local symmetry breaking even in the absence of long- or short-range ordering.[39] On the other hand, the fraction of HS and LS molecules is not always straightforward to extract from the Raman spectra. To obtain this information we have also acquired lattice parameter data of the crystals as a function of temperature and pressure, the spontaneous volume strain being proportional to the high spin fraction ($n_{HS} \propto e_V$) to a good approximation. Besides the thermal SCO, we have also explored the pressure-induced spin transition behavior in **1**. In a first approximation, the effect of an applied hydrostatic pressure is expected to be the same as the lowering of temperature, both stabilizing the LS state, characterized by reduced entropy and volume in comparison with the HS form.[1] Nevertheless, the effect of pressure on the SCO phenomenon often appears more intricate. For example, the hysteresis loop associated with the thermal SCO can exhibit either a decrease or an increase under pressure.[8] In other occasions, the application of pressure allowed separation of the SCO from coupled crystallographic phase transitions.[9,67] From a fundamental point of view, it is thus interesting to examine the effect of pressure on stepped phase transitions as well,[53] but this has been done in only a few instances and, in general, using only magnetometry detection.[68]

Experimental

Single crystals of **1** have been obtained according to previously described procedures.[62] Low temperature XRD measurements have been conducted between 100 and 300 K using a Bruker Kappa Apex II diffractometer with graphite-monochromated Mo-Kα radiation (λ = 0.71073 Å) and an Oxford Cryosystems Cryostream cooler device. High pressure XRD data were collected using an XtaLAB Synergy-S Rigaku diffractometer equipped with a hybrid photon counting Hypix-6000HE detector and a Mo microsource. The CrysAlisPro program suite was used for pre-experiment, DAC alignment, data collection, determination of the UB matrices, and initial data reduction.[69] Crystal structures were solved and refined using SHELXS and SHELXL programs.[70] Hydrogen atoms were located from geometry after each refinement cycle. The high-pressure diffraction experiments have been performed at room temperature using a One20DAC Almax-EasyLab wide-angle diamond anvil cell (DAC) equipped with diamonds of Boehler–Almax design and of a cullet diameter of 800 μm.[67] Stainless steel gaskets of 0.2 mm thickness with holes of *ca.* 0.3 mm in diameter have been prepared by spark-erosion. The fluorescence of ruby was used as a pressure gauge[71] and Daphne 7373 oil as the pressure-transmitting medium.[72] The uncertainty of the pressure values is estimated on the order of 0.5–1 kbar. Raman

spectra were acquired using an Xplora microspectrometer (Horiba) equipped with 532 and 638 nm lasers. The laser beam was focused on the sample with a long-working-distance objective (50×, numerical aperture = 0.5), which was also used to collect the scattered photons. The laser intensity (*ca.* 1 mW) was carefully adjusted to minimize unwanted laser-induced heating. During the experiments the orientation of the sample crystal was kept constant with respect to the polarization direction of the laser. Using a 2400 grooves per mm grating and a 100 μm slit, a spectral resolution of *ca.* 3 cm^{-1} was achieved. For high pressure Raman experiments the One20DAC was employed, whereas variable temperature Raman spectra were collected using a THMS600 heating–cooling stage (Linkam Scientific).

Results and discussion

Compound **1** displays a multistep transition between the pure low spin (S = 0, $^1A_{1g}$) and high spin (S = 2, $^5T_{2g}$) states when heated from 175 K to 275 K.[62] Lattice volume and orthorhombic (*Cccm*) lattice parameter variations through this transition, extracted from single-crystal XRD measurements, are shown in Fig. 2a and b, respectively. As it can be expected, the cell volume increases considerably upon heating due to the concomitant effects of the thermal expansion and the LS → HS transition. Ordinary thermal dilation is characterized by the volumetric coefficients of thermal expansion $\left(\alpha_V = \frac{dV}{V_0 dT}\right)$ of 7.2(2) × 10^{-5} K^{-1} and 1.2(1) × 10^{-4} K^{-1} in the LS and HS phases, respectively, whereas the SCO involves an *ca.* one order of magnitude higher thermal expansion, reaching peak values of *ca.* 10^{-3} K^{-1} near the transition temperatures. On the other hand, the cell axis lengths show distinct behaviors. The linear thermal expansion along the cell axes $\left(\alpha_i = \frac{di}{i_0 dT},\ i = a, b \text{ or } c\right)$ exhibits positive values along the a and b directions, but a negative linear thermal expansion (NLTE) behavior is apparent along the c-direction both in the HS and LS phases. The cell

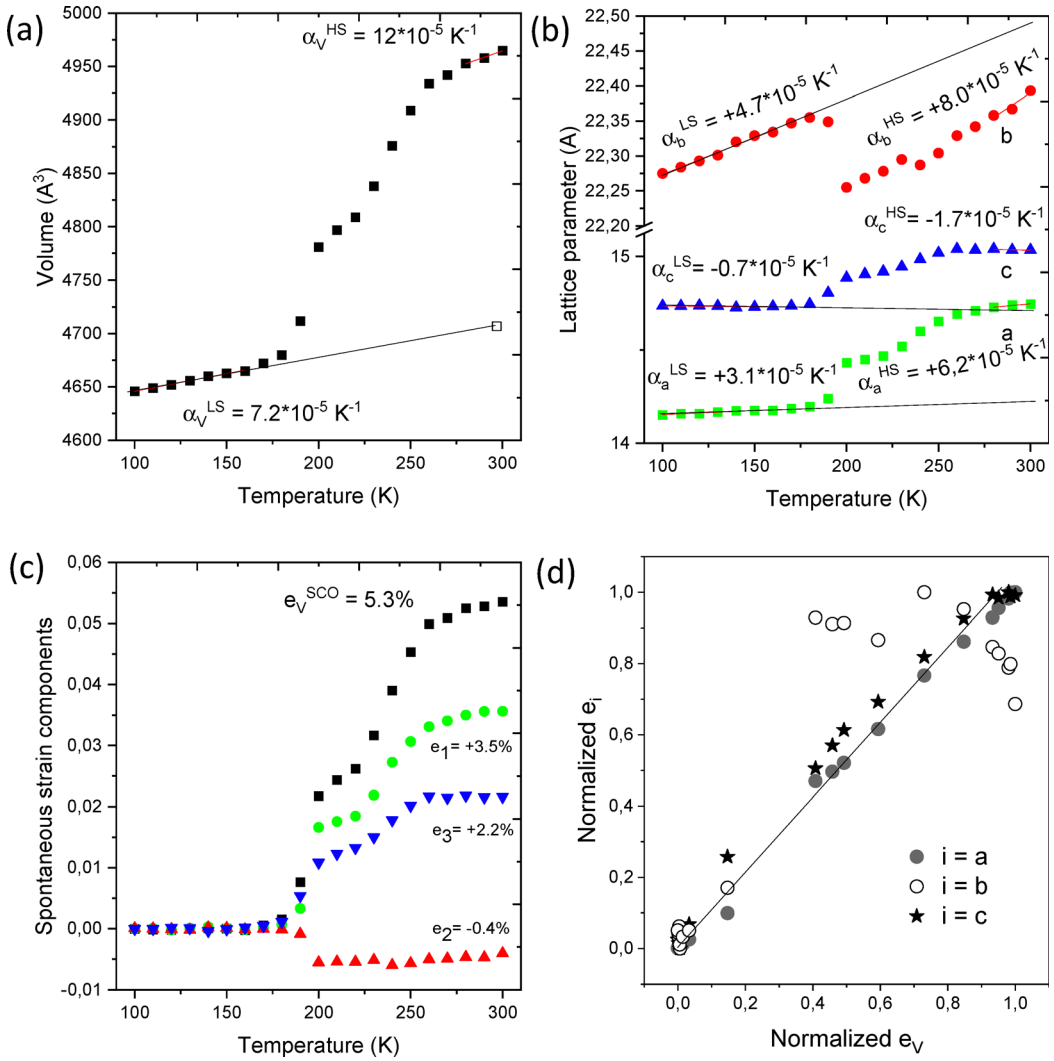

Fig. 2 (a) Cell volume, (b) lattice parameters and (c) transformation strain as a function of the temperature in compound **1**. (d) Variation of the individual strain components *vs.* the volume strain. Lines are linear fits to the data.

parameter variations are strongly anisotropic at the spin transition as well, but in this case an anomalous decrease of the *b*-axis length is observed when going to the HS phase, whereas an expansion occurs in the *a* and *c* directions. Nevertheless, we should stress that this type of 'anomalous' negative expansion of cell axis lengths is frequently encountered both on heating and on the SCO, in particular, in cyanometallate based frameworks.[66]

From the lattice parameter data we extracted the transformation strain characterizing the spin transition. To do this, we have extrapolated the lattice parameters of the LS phase to the entire temperature range (see Fig. 2a and b) and subtracted them from the total strain to obtain the neat transformation strain (in Voigt notation:[73] $e_1 = \Delta a/a_{LS} = 0.035$, $e_2 = \Delta b/b_{LS} = -0.004$, $e_3 = \Delta c/c_{LS} = 0.022$) (Fig. 2c). The sum of the individual strain components obtained from this analysis equals the volume strain ($e_1 + e_2 + e_3 = e_V = \Delta V/V_{LS} = 0.053$), thus providing confidence for the validity of the data treatment. One can also note that the plateau between the two steps of the SCO corresponds to the half of the volume strain (*i.e.* half-transition), in line with previous experimental observations. On the other hand, the two other steps at 1/4 and 3/4 transitions cannot be resolved in the present experiments. For isostructural transitions, such as the case of compound **1**, symmetry constraints do not arise and therefore the lowest-order coupling between the order parameter (*i.e.* the high spin fraction) and the transformation strain is bilinear.[52,53] Since higher-order coupling terms usually provide rather small contributions to the free energy, the relationship between n_{HS} and the different strain components for **1** is then expected to be linear:

$$n_{HS} \propto e_V \propto e_1 \propto e_2 \propto e_3 \quad (1)$$

As shown in Fig. 2d, this linear relationship is indeed verified between e_V, e_1 and e_3, but e_2 shows a clear deviation from the expected behavior. This aberration might be either the manifestation of higher-order couplings or the sign of a concurrent phenomenon, characterized by another order parameter. While we cannot discard the latter possibility, we suggest that the anomaly should be related to the manifestly weak bilinear coupling between the high spin fraction and the strain component e_2. Indeed, in such a case, one might expect that even a small higher order coupling may appear significant with respect to the weak lowest-order (bilinear) coupling term. Clearly, this finding represents only a minor deviation from the standard linear strain behavior in SCO materials and it reveals a subtle aspect of the SCO in **1**.

Raman spectra of **1** (excited at 532 nm) have been acquired from 150 to 293 K. Laser-induced heating of the sample was clearly evidenced by testing the effect of the laser intensity on the Raman spectra within the spin transition region. Based on this test, we have chosen a laser power of 1 mW, which provided a reasonable compromise between the Raman signal intensity and sample heating. Indeed, by comparing the SCO curves obtained from Raman and XRD measurements, an *ca.* 30 K heating of the sample by the laser could be estimated. This does not alter, however, the observed spectral behavior; it merely downshifts the SCO curve *vs.* the 'real' transition temperature (seen for example in magnetometry). As can be expected for such anisotropic samples, the Raman signal was also dependent on the crystal orientation. Unfortunately, it was not possible to orient the orthorhombic axes parallel to the laser polarization direction inside the pressure cell (*vide infra*). For this reason, temperature scans were run simply in such a way to acquire Raman spectra on the crystal in similar (arbitrary) orientation to that studied under variable pressure. Fig. 3a displays selected Raman spectra acquired in the low-frequency range (100–550 cm^{-1}) for the pure LS (150 K), pure HS (300 K) and mixed HS + LS (200 K) states. Spectra recorded in a wider spectral range are shown in the SI, in Section S1. The Raman spectra at frequencies between *ca.* 600 and 1600 cm^{-1} are dominated by vibrational modes of the AnPy ligand and the NO_2bz guest molecule. Whereas these modes remain relatively insensitive to the spin state change of the central metal ion, in agreement with the general expectation, the low-frequency LS and HS spectra appear drastically different. Indeed, this low-frequency region comprises primarily vibrational modes associated with displacements of heavy metal ions (Fe^{2+} and Ag^{+}), as well as, presumably, a few libration modes of guest molecules and ligands. It is well known that vibrational frequencies associated with different modes of the FeN_6 coordination octahedra, in particular the Fe–N stretchings, exhibit considerable spectral redshifts when going from the LS to the HS state, which arises due to the population of antibonding orbitals in the former.[1] In addition, in ferrous cyanometallate SCO complexes the frequencies of the cyanometallate group were shown to also display sizeable changes at the spin transition, due to couplings with the Fe–N vibrations.[74] Remarkably, the Raman spectrum recorded in the mixed HS + LS state in the plateau region does not appear as a mixture of the HS and LS spectra. Indeed, several Raman peaks corresponding to the neat (HS or LS) phases show a complete extinction in the plateau region, whereas additional peaks appear. This is clearly seen in Fig. 3b, through the temperature dependence of the peaks at 190 (resp. 296) cm^{-1}, the former (resp. latter) appearing only in the LS (resp. HS) phases, whereas the one at 220 cm^{-1} can be observed exclusively in the plateau region. It is worth mentioning that similar observations could be obtained from other crystals of **1** and using different laser excitation wavelengths, which are shown in the SI, Section S1. This distinct nature of the intermediate HS–LS state can be nicely depicted in the low–frequency Raman maps in Fig. 3c and d. On the whole, these spectral features thus reveal clearly a local symmetry-breaking, which we can interpret as the predominance of HS–LS neighbors at the detriment of HS–HS or LS–LS ones. The present results for complex **1** are reminiscent of those previously reported for the binuclear complex $[Fe(bt)(NCS)_2]_2$bpym[39] and are clearly different from 'ordinary' SCO complexes, which display in general a co-existence of LS and HS spectral features at the half-transition. This situation also resembles to the case of the compound $[Fe(dpbtz)(Au(CN)_2)_2]\cdot 0.5chry\cdot 1.5MeCN$ (dpbtz = 4,7-di(4-pyridyl)-2,1,3-benzothiadiazole; chry = chrysene; MeCN = acetonitrile) reported by Windsor *et al.* in ref. 65. The authors proposed that the strong positional disorder of the guest molecules within the voids, which is also the

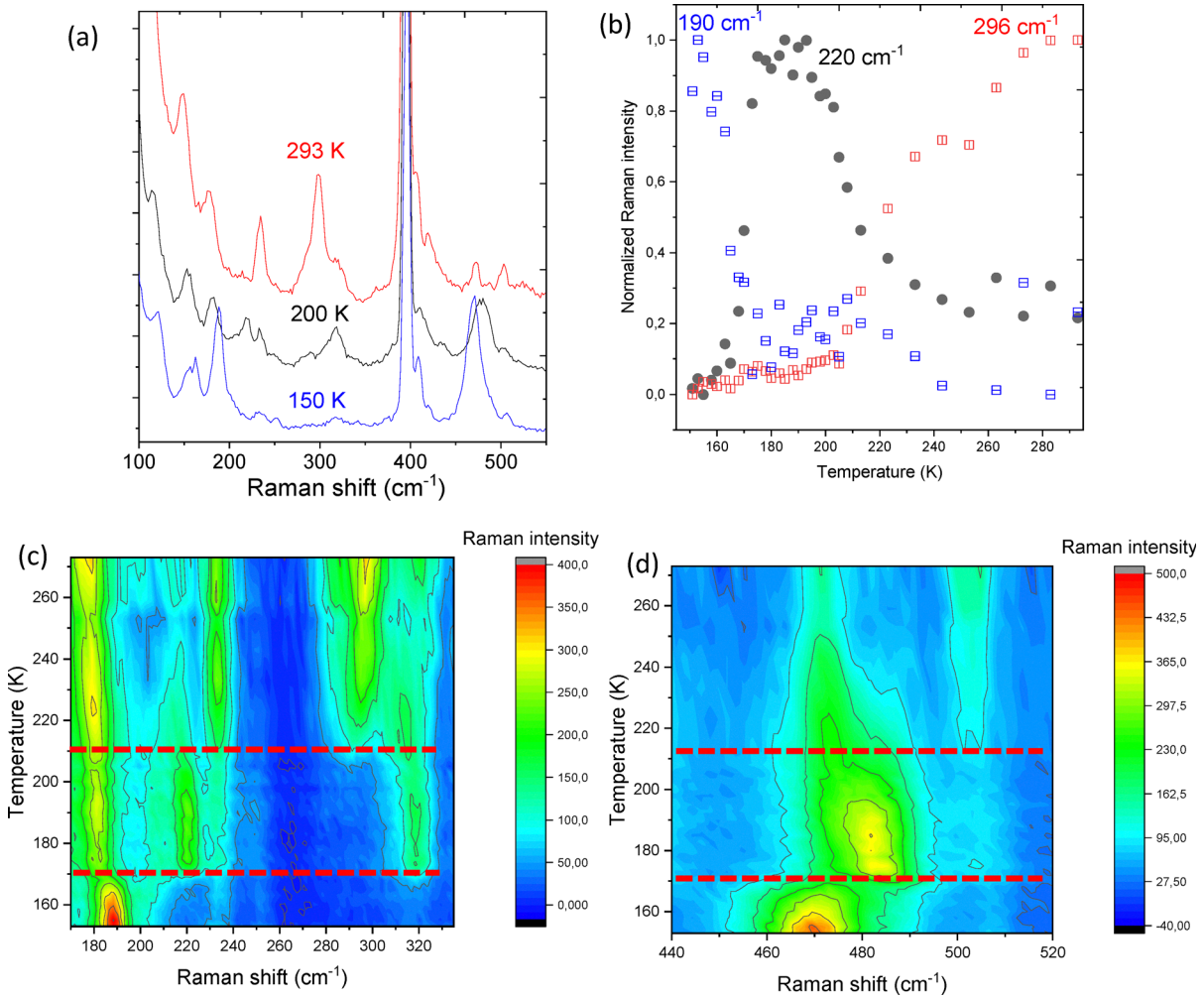

Fig. 3 (a) Low-frequency Raman spectra of a crystal of **1** at selected temperatures. (b) Temperature dependence of the normalized intensity of selected Raman modes. (c) and (d) Temperature–frequency maps of the Raman spectral intensities through the stepped spin transition in **1** in the low-frequency region. The dashed horizontal lines delimit the half-transition plateau region of the SCO, revealing three distinct Raman spectra corresponding to the pure HS, mixed (50–50%) HS–LS and pure LS forms.

case of compound **1**, gives rise to a disorder of local environments with different local ligand fields, thus impeding a long-range periodic distribution of HS–LS sites, which could be detectable by XRD.

Having characterized the stepped thermal SCO phenomenon in **1**, we have extended our investigation to the effects of an applied hydrostatic pressure. As mentioned above, increasing pressure is expected to have a similar effect on the spin state of the compound as decreasing temperature. However, when analyzing lattice parameter variations, one significant difference with respect to the thermal expansion is that the compressibility displays a non-linear behavior, which means that more care is needed to extrapolate the LS lattice parameters within the HS stability field. Another practical issue is related to the fact that the pressure steps in the DAC are rather crude, providing a much lower resolution of the pressure-induced spin transition, when compared to the thermally induced SCO. As shown in Fig. 4a, the cell volume decreases by *ca.* 15% at 16 kbar due to the combined effects of the ordinary mechanical compression and the HS → LS transition. Above this pressure we noted the onset of a degradation of the crystal quality. The spin transition is clearly manifested by the non-monotonous shrinking of the volume and lattice parameters (Fig. 4b) between *ca.* 1 and 6 kbar applied pressure. Due to this early onset of the pressure-induced SCO, the compressibility of the lattice in the HS phase could not be assessed.

In the LS state, the bulk modulus $\left(B_V = -\frac{V_0 \mathrm{d}p}{\mathrm{d}V}\right)$, extracted from the *P*–*V* data using the second-order Birch–Murnaghan equation of state,[75] is *ca.* 12(1) GPa, which is comparable with values reported for other SCO materials.[76] Similar to the thermal expansion behavior, the unidirectional bulk moduli along the cell axes $\left(B_i = -\frac{i_0 \mathrm{d}p}{\mathrm{d}i},\ i = a, b \text{ or } c\right)$ exhibit strongly anisotropic behavior. Notably, along the *a*-axis the material is essentially incompressible in the LS phase, and the data suggest that a negative linear compressibility (NLC) behavior might occur along this direction in the HS phase. The values of

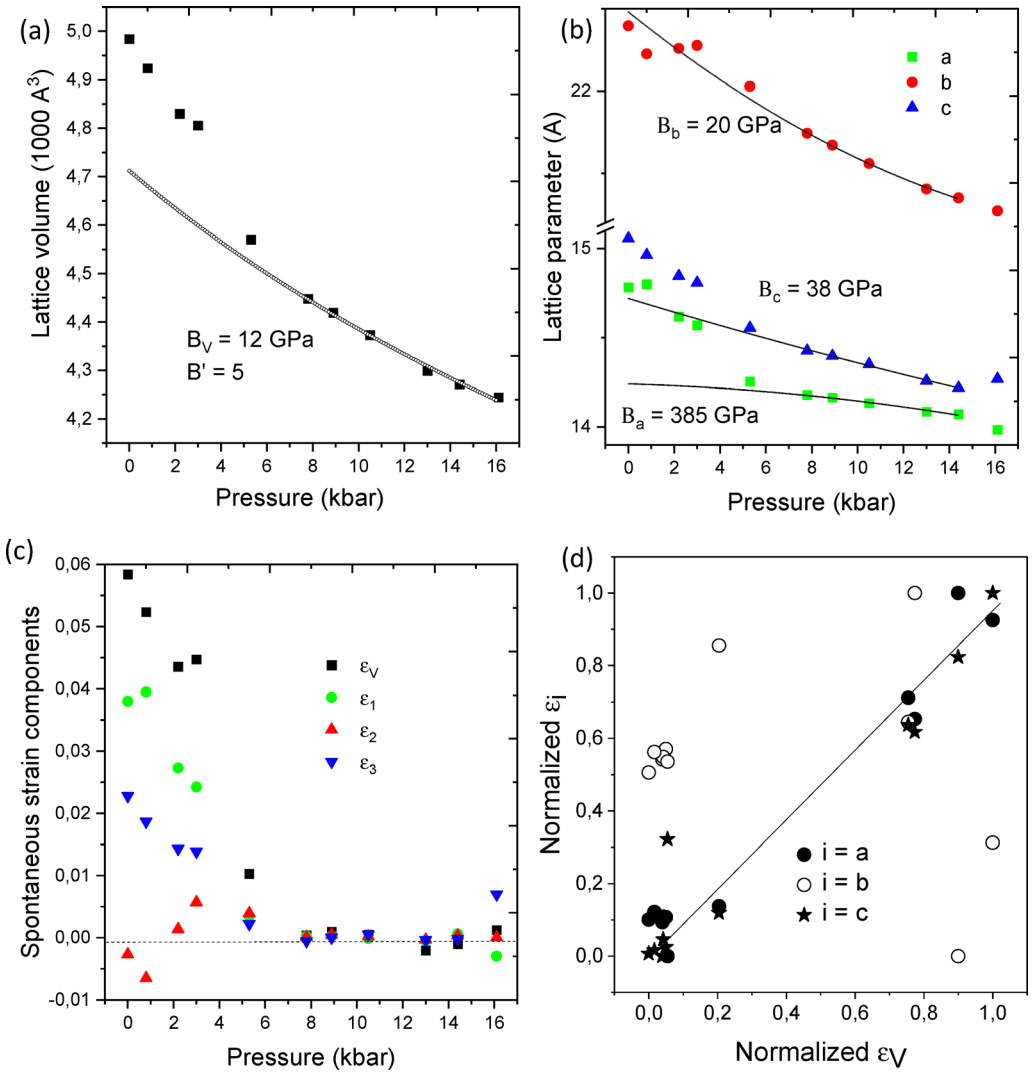

Fig. 4 (a) Cell volume, (b) lattice parameters and (c) transformation strain as a function of the pressure in compound **1** at 295 K. (d) Variation of the individual strain components *vs.* the volume strain under pressure. Lines are polynomial fits to the data (first or second order).

B_i were obtained using a second-order polynomial fit,[77] which was also used to extract the pressure-induced transformation strain values (e_i), depicted in Fig. 4c. The validity of the fitting process is supported by the good match between the linear and volumetric bulk moduli, which fulfills the expected relationship $\left(\frac{1}{B_V} = \sum_i \frac{1}{B_i}\right)$. On the whole, the pressure- and temperature-induced spin transitions are characterized by closely comparable unit cell deformations. Notably, one can observe an anomalous behavior of the strain component e_2 under pressure as well (Fig. 4d). The values of e_i indicate that the SCO is complete under *ca.* 6 kbar applied pressure. Remarkably, a plateau in the spin transition can be depicted between *ca.* 2 and 3 kbar, revealing that the pressure-induced SCO occurs also in a step-wise manner. This is clearly seen in the behavior of the strain components e_V, e_1 and e_3 in Fig. 4c. From the lattice parameters alone, however, it is not possible to establish with confidence the fraction of LS centers neither in the plateau, nor at the end of the pressure-induced SCO. For this reason, we collected complete structural data and resolved the structure of our compound under 2 and 6 kbar compression (see the detailed crystallographic data in the SI). As shown in Table 1, the Fe–N distances assessed at 6 and 2 kbar match – within the experimental uncertainty – those measured in the thermally-induced LS state (120 K) and in the thermal half-transition (210 K), respectively. This finding proves that the pressure-induced SCO leads to a fully populated LS state at 6 kbar, whereas the 2–3 kbar plateau corresponds to a 50–50% mixture of HS and LS species. (N.B. This analysis is based on the fact that such relatively small pressure and temperature variations do not sizably alter the Fe–N distances in the absence of the SCO phenomenon.[78])

Raman spectra of **1** under hydrostatic pressure have been acquired through three compression series up to 13 kbar applied pressure with steps of *ca.* 1–2 kbar. Due to the presence of the pressure transmitting medium and the diamond anvils, these spectra are more noisy than those recorded at ambient pressure (see Section S2 in the SI for the full set of collected

Table 1 Fe–N distances in **1** at selected temperatures and pressures. Atmospheric pressure structural data have been taken from ref. 62

Temperature (K)	Pressure	Fe–N1 distance (axial) (Å)	Fe–N2 distance (equatorial) (Å)
293	6 kbar	2.014 (10)	1.936 (5)
293	2 kbar	2.11 (2)	2.017 (12)
290	1 atm	2.228 (6)	2.139 (5)
210	1 atm	2.10 (1)	2.039 (7)
120	1 atm	2.000 (6)	1.932 (4)

high pressure Raman spectra). In particular, the low-frequency spectral features are of rather weak intensity. For this reason, we extended the spectrum acquisition up to the CN stretching frequencies near 2170 cm^{-1}. In fact, the CN modes exhibited only a minor shift at the spin transition, from *ca.* 2171 to 2169 cm^{-1}, which renders them, at first sight, less enlightening. This lack of sensitivity of the CN stretching frequencies is likely a consequence of opposed effects of σ donation and π back-bonding on the electron density of antibonding CN orbitals, both being enhanced in the LS state of the ferrous ions. In addition, we must note that the application of pressure also leads to an increase of the CN mode frequencies, even in the absence of SCO. Nevertheless, it turned out that the change of the linewidth of the CN stretching peak as a function of pressure provides a useful diagnostic feature of the stepped spin transition. Indeed, as shown in Fig. 5a, the linewidth of this Raman peak broadens considerably in an intermediate pressure range between *ca.* 1 and 5 kbar, thus delimiting the region of coexistence of HS and LS molecules, in a reasonably good agreement with the XRD results obtained under pressure. Despite the weak intensity of the low-frequency Raman peaks in the pressure cell, importantly, one can observe the same general tendencies as in the temperature dependent spectra. The Raman spectrum in the plateau (*e.g.* 1.9 kbar), shown in Fig. 5b, is clearly not the sum of the pure HS (0 kbar) and LS (5.8 kbar) spectra. Notably, the HS marker peaks at 296 and 154 cm^{-1} disappear upon the application of *ca.* 2–3 kbar for the detriment of new peaks at 220 and 158 cm^{-1} in the intermediate (HS + LS) form, which vanish when the pressure reaches 6 kbar, wherein the LS marker peak at 190 cm^{-1} emerges. This similarity with the temperature induced changes in the Raman spectra thus indicates a local symmetry breaking in the course of the pressure-induced spin transition, which thus appears analogous to the thermal SCO.

Conclusions

The main finding of the present work is the observation, *via* Raman spectroscopy, of a local symmetry breaking at the plateau of the stepped temperature-induced spin transition in the complex $\{Fe^{II}(AnPy)_2[Ag^{I}(CN)_2]_2\}\cdot NO_2bz$, indicating the predominance of HS–LS neighbors in the crystal. We believe that these HS–LS pairs do not adopt a long-range order because of the considerable positional disorder of the guest NO_2bz molecules in the lattice. Using high pressure XRD we could also establish a two-step sequence in the course of the pressure-induced SCO with a half-transition plateau between *ca.* 2 and 4 kbar, whereas the complete transformation to the LS state is reached at *ca.* 6 kbar. Despite the less comprehensive experimental data obtained under pressure, both the spontaneous strain components and the Raman spectra showed comparable changes under compression and cooling, suggesting that the stepped transitions are closely analogous under these different external stimuli. These initial observations open interesting perspectives for further studies, which include a more refined

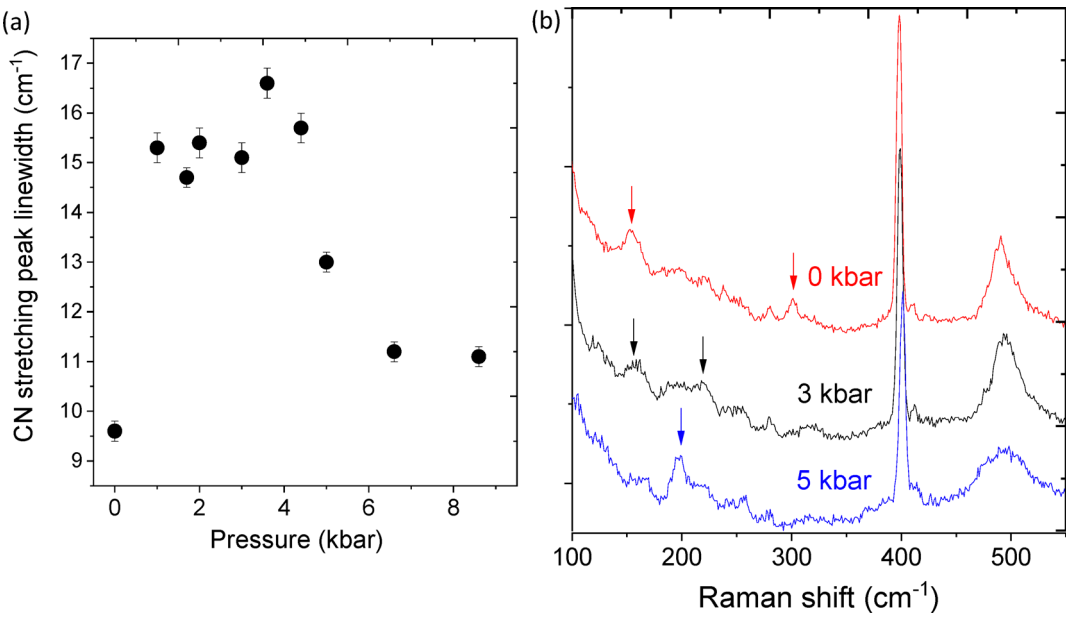

Fig. 5 (a) Pressure dependence of the full width at half maximum of the CN stretching peak in the Raman spectrum of **1**. (b) Low-frequency Raman spectra of a crystal of **1** at selected applied pressures.

analysis of the intermediate steps of the SCO, the assignment of the low-frequency Raman peaks using isotope substitutions coupled to quantum chemical calculations,[79] the extension of this analysis to the light-induced spin transition as well as to other members of this family of complexes.

During this work we used single crystal XRD to quantify the progress of the spin transition as a function of the temperature and pressure *via* the analysis of the lattice parameters. Using these data we have not only extracted the transformation strain, but also the coefficients of thermal expansion (both HS and LS) as well as the linear bulk moduli (LS), each revealing pronounced, but distinct anisotropies. The assessment of this type of information, characterizing the thermo-elastic properties of SCO complexes, is highly important not only for structure–property correlations, but also for their potential applications in mechanical actuators[80] and mechanocaloric devices.[81]

Conflicts of interest

The authors declare no competing financial interest.

Data availability

The data supporting this article have been included as part of the supplementary information (SI). Supporting information: all variable-temperature and variable-pressure Raman spectra as well as complementary crystallography information (PDF). See DOI: **https://doi.org/10.1039/d5cp02831k**.

CCDC 2452238 and 2452239 contain the supplementary crystallographic data for this paper.[82a,b]

Acknowledgements

This work has received funding from the European Research Council (ERC) under the European Union's Horizon 2020 research and innovation program (grant agreement no. 101019522) as well as from the European Regional Development Fund (ERDF), the Region Occitanie, and the company Rigaku Corporation (PRRI project NANOMAT). MN is grateful for a PhD grant of MESRI (Ministère de l'Enseignement supérieur, de la Recherche et de l'Innovation). RTC acknowledges the support from the Generalitat Valenciana (CIAPOS/2023/374). The work received financial support from the grant PID2023-150732NB-I00 funded by the Spanish MI-CIU/AEI/10.13039/501100011033 and FEDER/UE. The authors are undebted to Damian Paliwoda for the training provided for the use of the high pressure equipment.

References

1 P. Gütlich, A. Hauser and H. Spiering, *Angew. Chem., Int. Ed. Engl.*, 1994, **33**, 2024–2054.
2 P. Gütlich and H. A. Goodwin, in *Spin Crossover in Transition Metal Compounds I*, ed. P. Gütlich and H. A. Goodwin, Springer, Berlin, Heidelberg, 2004, pp. 1–4.
3 A. Bousseksou, G. Molnár, L. Salmon and W. Nicolazzi, *Chem. Soc. Rev.*, 2011, **40**, 3313–3335.
4 M. A. Halcrow, *Spin-Crossover Materials: Properties and Applications*, John Wiley & Sons, 2013.
5 J. A. Real, A. B. Gaspar and M. C. Muñoz, *Dalton Trans.*, 2005, 2062–2079.
6 A. Hauser, in *Spin Crossover in Transition Metal Compounds I*, ed. P. Gütlich and H. A. Goodwin, Springer, Berlin, Heidelberg, 2004, pp. 49–58.
7 W. Nicolazzi and A. Bousseksou, *C. R. Chim.*, 2018, **21**, 1060–1074.
8 H. Spiering, K. Boukheddaden, J. Linares and F. Varret, *Phys. Rev. B: Condens. Matter Mater. Phys.*, 2004, **70**, 184106.
9 E. Collet and G. Azzolina, *Phys. Rev. Mater.*, 2021, **5**, 044401.
10 P. Guionneau, *Dalton Trans.*, 2013, **43**, 382–393.
11 S. Pillet, *J. Appl. Phys.*, 2021, **129**, 181101.
12 Y.-Y. Peng, S.-G. Wu, Y.-C. Chen, W. Liu, G.-Z. Huang, Z.-P. Ni and M.-L. Tong, *Inorg. Chem. Front.*, 2020, **7**, 1685–1690.
13 E. V. Ivanov, PhD thesis, Institute of Technical Physics, Moscow, USSR, 1969.
14 Y. Garcia, O. Kahn, L. Rabardel, B. Chansou, L. Salmon and J. P. Tuchagues, *Inorg. Chem.*, 1999, **38**, 4663–4670.
15 E. Collet and P. Guionneau, *C. R. Chim*, 2018, **21**, 1133–1151.
16 H. Köppen, E. W. Müller, C. P. Köhler, H. Spiering, E. Meissner and P. Gütlich, *Chem. Phys. Lett.*, 1982, **91**, 348–352.
17 D. Chernyshov, M. Hostettler, K. W. Törnroos and H.-B. Bürgi, *Angew. Chem., Int. Ed.*, 2003, **42**, 3825–3830.
18 A. Bousseksou, J. Nasser, J. Linares, K. Boukheddaden and F. Varret, *J. Phys.*, 1992, **2**, 1381–1403.
19 E. Trzop, D. Zhang, L. Piñeiro-Lopez, F. J. Valverde-Muñoz, M. Carmen Muñoz, L. Palatinus, L. Guerin, H. Cailleau, J. A. Real and E. Collet, *Angew. Chem., Int. Ed.*, 2016, **55**, 8675–8679.
20 S. Bonnet, G. Molnár, J. Sanchez Costa, M. A. Siegler, A. L. Spek, A. Bousseksou, W.-T. Fu, P. Gamez and J. Reedijk, *Chem. Mater.*, 2009, **21**, 1123–1136.
21 V. A. Money, C. Carbonera, J. Elhaïk, M. A. Halcrow, J. A. K. Howard and J.-F. Létard, *Chem. - Eur. J.*, 2007, **13**, 5503–5514.
22 C.-F. Sheu, S.-M. Chen, S.-C. Wang, G.-H. Lee, Y.-H. Liu and Y. Wang, *Chem. Commun.*, 2009, 7512–7514.
23 J. Luan, J. Zhou, Z. Liu, B. Zhu, H. Wang, X. Bao, W. Liu, M.-L. Tong, G. Peng, H. Peng, L. Salmon and A. Bousseksou, *Inorg. Chem.*, 2015, **54**, 5145–5147.
24 N. Bréfuel, E. Collet, H. Watanabe, M. Kojima, N. Matsumoto, L. Toupet, K. Tanaka and J.-P. Tuchagues, *Chem. - Eur. J.*, 2010, **16**, 14060–14068.
25 K. Nakano, S. Kawata, K. Yoneda, A. Fuyuhiro, T. Yagi, S. Nasu, S. Morimoto and S. Kaizaki, *Chem. Commun.*, 2004, 2892–2893.
26 J. J. M. Amoore, C. J. Kepert, J. D. Cashion, B. Moubaraki, S. M. Neville and K. S. Murray, *Chem. - Eur. J.*, 2006, **12**, 8220–8227.
27 J.-B. Lin, W. Xue, B.-Y. Wang, J. Tao, W.-X. Zhang, J.-P. Zhang and X.-M. Chen, *Inorg. Chem.*, 2012, **51**, 9423–9430.
28 V. Martínez, A. B. Gaspar, M. C. Muñoz, G. V. Bukin, G. Levchenko and J. A. Real, *Chem. - Eur. J.*, 2009, **15**, 10960–10971.
29 G. Agustí, A. B. Gaspar, M. C. Muñoz and J. A. Real, *Inorg. Chem.*, 2007, **46**, 9646–9654.

30 W. Liu, Y.-Y. Peng, S.-G. Wu, Y.-C. Chen, Md. N. Hoque, Z.-P. Ni, X.-M. Chen and M.-L. Tong, *Angew. Chem., Int. Ed.*, 2017, **56**, 14982–14986.
31 J. E. Clements, J. R. Price, S. M. Neville and C. J. Kepert, *Angew. Chem., Int. Ed.*, 2016, **55**, 15105–15109.
32 C.-F. Sheu, S. Pillet, Y.-C. Lin, S.-M. Chen, I.-J. Hsu, C. Lecomte and Y. Wang, *Inorg. Chem.*, 2008, **47**, 10866–10874.
33 E. Collet, H. Watanabe, N. Bréfuel, L. Palatinus, L. Roudaut, L. Toupet, K. Tanaka, J.-P. Tuchagues, P. Fertey, S. Ravy, B. Toudic and H. Cailleau, *Phys. Rev. Lett.*, 2012, **109**, 257206.
34 C. Mariette, E. Trzop, S. Zerdane, P. Fertey, D. Zhang, F. J. Valverde-Muñoz, J.-A. Real and E. Collet, *Acta Crystallogr., Sect. B: Struct. Sci., Cryst. Eng. Mater.*, 2017, **73**, 660–668.
35 S. M. Neville, B. A. Leita, G. J. Halder, C. J. Kepert, B. Moubaraki, J.-F. Létard and K. S. Murray, *Chem. – Eur. J.*, 2008, **14**, 10123–10133.
36 C. Mariette, E. Trzop, J.-Y. Mevellec, A. Boucekkine, A. Ghoufi, G. Maurin, E. Collet, M. C. Muñoz, J. A. Real and B. Toudic, *Phys. Rev. B*, 2020, **101**, 134103.
37 J. A. Real, H. Bolvin, A. Bousseksou, A. Dworkin, O. Kahn, F. Varret and J. Zarembowitch, *J. Am. Chem. Soc.*, 1992, **114**, 4650–4658.
38 V. Ksenofontov, H. Spiering, S. Reiman, Y. Garcia, A. B. Gaspar, N. Moliner, J. A. Real and P. Gütlich, *Chem. Phys. Lett.*, 2001, **348**, 381–386.
39 N. O. Moussa, G. Molnár, S. Bonhommeau, A. Zwick, S. Mouri, K. Tanaka, J. A. Real and A. Bousseksou, *Phys. Rev. Lett.*, 2005, **94**, 107205.
40 N. O. Moussa, E. Trzop, S. Mouri, S. Zein, G. Molnár, A. B. Gaspar, E. Collet, M. Buron-Le Cointe, J. A. Real, S. Borshch, K. Tanaka, H. Cailleau and A. Bousseksou, *Phys. Rev. B: Condens. Matter Mater. Phys.*, 2007, **75**, 054101.
41 N. Ortega-Villar, M. C. Muñoz and J. A. Real, *Magnetochemistry*, 2016, **2**, 16.
42 M. J. Murphy, K. A. Zenere, F. Ragon, P. D. Southon, C. J. Kepert and S. M. Neville, *J. Am. Chem. Soc.*, 2017, **139**, 1330–1335.
43 D. Boinnard, A. Bousseksou, A. Dworkin, J. M. Savariault, F. Varret and J.-P. Tuchagues, *Inorg. Chem.*, 1994, **33**, 271–281.
44 D. Chernyshov, N. Klinduhov, K. W. Törnroos, M. Hostettler, B. Vangdal and H.-B. Bürgi, *Phys. Rev. B: Condens. Matter Mater. Phys.*, 2007, **76**, 014406.
45 M. Mikolasek, W. Nicolazzi, F. Terki, G. Molnár and A. Bousseksou, *Chem. Phys. Lett.*, 2017, **678**, 107–111.
46 M. Nishino, Y. Singh, K. Boukheddaden and S. Miyashita, *J. Appl. Phys.*, 2021, **130**, 141102.
47 E. M. Hernández, S. Zheng, H. J. Shepherd, D. S. Yufit, K. Ridier, S. Bedoui, W. Nicolazzi, V. Velázquez, S. Bonnet, G. Molnár and A. Bousseksou, *J. Phys. Chem. C*, 2016, **120**, 27608–27617.
48 R. A. Bari and J. Sivardière, *Phys. Rev. B*, 1972, **5**, 4466–4471.
49 R. Jakobi, H. Spiering and P. Gütlich, *J. Phys. Chem. Solids*, 1992, **53**, 267–275.
50 H. Romstedt, H. Spiering and P. Gütlich, *J. Phys. Chem. Solids*, 1998, **59**, 1353–1362.
51 A. B. Koudriavtsev, *Chem. Phys.*, 1999, **241**, 109–126.
52 D. Chernyshov, H.-B. Bürgi, M. Hostettler and K. W. Törnroos, *Phys. Rev. B: Condens. Matter Mater. Phys.*, 2004, **70**, 094116.
53 G. Azzolina, R. Bertoni and E. Collet, *J. Appl. Phys.*, 2021, **129**, 085106.
54 A. Bousseksou, F. Varret and J. Nasser, *J. Phys.*, 1993, **3**, 1463–1473.
55 K. Boukheddaden, J. Linares, R. Tanasa and C. Chong, *J. Phys.: Condens. Matter*, 2007, **19**, 106201.
56 H. Watanabe, K. Tanaka, N. Bréfuel, H. Cailleau, J.-F. Létard, S. Ravy, P. Fertey, M. Nishino, S. Miyashita and E. Collet, *Phys. Rev. B*, 2016, **93**, 014419.
57 M. Paez-Espejo, M. Sy and K. Boukheddaden, *J. Am. Chem. Soc.*, 2016, **138**, 3202–3210.
58 J. Cruddas and B. J. Powell, *Inorg. Chem. Front.*, 2020, **7**, 4424–4437.
59 M. Ndiaye, Y. Singh, H. Fourati, M. Sy, B. Lo and K. Boukheddaden, *J. Appl. Phys.*, 2021, **129**, 153901.
60 S. Vela and H. Paulsen, *Inorg. Chem.*, 2018, **57**, 9478–9488.
61 G. Ruzzi, J. Cruddas and B. J. Powell, *Mater. Adv.*, 2024, **5**, 2057–2068.
62 R. Turo-Cortés, M. Meneses-Sánchez, T. Delgado, C. Bartual-Murgui, M. C. Muñoz and J. A. Real, *J. Mater. Chem. C*, 2022, **10**, 10686–10698.
63 T. Kosone, I. Tomori, C. Kanadani, T. Saito, T. Mochida and T. Kitazawa, *Dalton Trans.*, 2010, **39**, 1719–1721.
64 O. I. Kucheriv, I. O. Fritsky and I. A. Gural'skiy, *Inorg. Chim. Acta*, 2021, **521**, 120303.
65 H. J. Windsor, W. Lewis, S. M. Neville, S. G. Duyker, D. M. D'Alessandro and C. J. Kepert, *Chem. Commun.*, 2022, **58**, 13127–13130.
66 M. C. Muñoz and J. A. Real, *Coord. Chem. Rev.*, 2011, **255**, 2068–2093.
67 D. Paliwoda, L. Vendier, W. Nicolazzi, G. Molnár and A. Bousseksou, *Inorg. Chem.*, 2022, **61**, 15991–16002.
68 A. B. Gaspar, G. Molnár, A. Rotaru and H. J. Shepherd, *C. R. Chim*, 2018, **21**, 1095–1120.
69 *CrysAlisPro, Version 1.171.33.66*, Oxford Diffraction Ltd.
70 G. M. Sheldrick, *Acta Crystallogr., Sect. A: Found. Crystallogr.*, 2008, **64**, 112–122.
71 G. J. Piermarini, S. Block, J. D. Barnett and R. A. Forman, *J. Appl. Phys.*, 1975, **46**, 2774–2780.
72 N. Tateiwa and Y. Haga, *Rev. Sci. Instrum.*, 2009, **80**, 123901.
73 M. A. Carpenter, E. K. H. Salje and A. Graeme-Barber, *Eur. J. Mineral.*, 1998, 621–691.
74 G. Molnár, V. Niel, A. B. Gaspar, J.-A. Real, A. Zwick, A. Bousseksou and J. J. McGarvey, *J. Phys. Chem. B*, 2002, **106**, 9701–9707.
75 R. J. Angel, *Rev. Mineral. Geochem.*, 2000, **39**, 85–104.
76 M. Mikolasek, M. D. Manrique-Juarez, H. J. Shepherd, K. Ridier, S. Rat, V. Shalabaeva, A.-C. Bas, I. E. Collings, F. Mathieu, J. Cacheux, T. Leichle, L. Nicu, W. Nicolazzi, L. Salmon, G. Molnár and A. Bousseksou, *J. Am. Chem. Soc.*, 2018, **140**, 8970–8979.
77 A. B. Cairns and A. L. Goodwin, *Phys. Chem. Chem. Phys.*, 2015, **17**, 20449–20465.
78 P. Guionneau, M. Marchivie, G. Bravic, J.-F. Létard and D. Chasseau, in *Spin Crossover in Transition Metal Compounds II*, ed. P. Gütlich and H. A. Goodwin, Springer, Berlin, Heidelberg, 2004, pp. 97–128.

79 V. K. Pálfi, T. Guillon, H. Paulsen, G. Molnár and A. Bousseksou, *C. R. Chim*, 2005, **8**, 1317–1325.
80 H. J. Shepherd, I. A. Gural'skiy, C. M. Quintero, S. Tricard, L. Salmon, G. Molnár and A. Bousseksou, *Nat. Commun.*, 2013, **4**, 2607.
81 S. P. Vallone, A. N. Tantillo, A. M. dos Santos, J. J. Molaison, R. Kulmaczewski, A. Chapoy, P. Ahmadi, M. A. Halcrow and K. G. Sandeman, *Adv. Mater.*, 2019, **31**, 1807334.
82 (*a*) Y. Remili, M. Nasimsobhan, R. Turo-Cortés, L. Vendier, C. Bartual-Murgui, G. Molnár, A. Bousseksou and J. A. Real, CCDC 2452238: Experimental Crystal Structure Determination, 2025, DOI: 10.5517/ccdc.csd.cc2n9rg6; (*b*) Y. Remili, M. Nasimsobhan, R. Turo-Cortés, L. Vendier, C. Bartual-Murgui, G. Molnár, A. Bousseksou and J. A. Real, CCDC 2452239: Experimental Crystal Structure Determination, 2025, DOI: 10.5517/ccdc.csd.cc2n9rh7.